Knowledge-Aided InSAR Phase Unwrapping Approach

Hanwen Yu, *Senior Member, IEEE*, and Xie Hu, *Member, IEEE*

***Abstract*— 2-D phase unwrapping (PU) is one of the biggest challenges in synthetic aperture radar (SAR) interferometry (InSAR) processing. As an ill-posed problem, the performance of the traditional algorithmic model-based 2-D PU algorithms is not guaranteed to be correct with rapid ground deformation or topographic changes. An increasing number of remote sensing observations collected by different sensors (e.g., LiDAR and GPS) provides new opportunities to assist the traditional 2-D InSAR PU by reducing the nondeterminacy. In this article, we propose a novel knowledge-aided PU (KAPU) approach. KAPU compiles different prior knowledge from different sources with InSAR observations simultaneously through an integer programming model. More importantly, the mathematical proof demonstrates that the constraint of the optimization model of KAPU is totally unimodular, so KAPU can be efficiently solved without having to have the constraint that the ambiguity number is an integer. Theoretical analysis and extensive experimental results illustrate that KAPU outperforms the existing model-based 2-D InSAR PU algorithms on digital elevation model (DEM) generation and surface deformation estimation.**

***Index Terms*— Phase unwrapping (PU), prior knowledge, synthetic aperture radar interferometry (InSAR), supervised processing.**

I. Introduction

SYNTHETIC aperture radar (SAR) interferometry (InSAR) is one of the microwave remote sensing tools featured with highly accurate measurement on the digital elevation model (DEM) and ground deformation [1]–[4]. In essence, InSAR measurements rely on the absolute phase changes between SAR acquisitions from slightly different positions [5]. The absolute phase consists of the wrapped phase and an ambiguity number of 2π (1).

$$\varphi(s) = \psi(s) - 2k(s)\pi, \quad k(s) \in \text{integer} \tag{1}$$

Manuscript received December 31, 2020; revised February 23, 2021; accepted April 10, 2021. This work was supported by the startup funding to Xie Hu at the University of Houston, the National Science Fund for Distinguished Young Scholars under Grant 61825105 and the National Natural Science Foundation of China under Grant 42071438. *(Corresponding author: Hanwen Yu.)*

Hanwen Yu was with the Department of Civil and Environmental Engineering, University of Houston, Houston, TX 77204 USA. He is now with the School of Resources and Environment, University of Electronic Science and Technology of China, Chengdu 611731, China (e-mail: yuhanwenxd@gmail.com).

Xie Hu is with the Department of Civil and Environmental Engineering, University of Houston, Houston, TX 77204 USA, and also with the National Center for Airborne Laser Mapping, University of Houston, Houston, TX 77204 USA.

Digital Object Identifier 10.1109/TGRS.2021.3081039

where $k(s)$, $\varphi(s)$, and $\psi(s)$ represent the ambiguity number, the wrapped phase and the absolute phase of the sth pixel in the interferogram.

InSAR imagery only provides $\varphi(s)$. Phase unwrapping (PU) aims at solving $\psi(s)$, which is an ill-posed problem since both $\psi(s)$ and $k(s)$ are unknown. In order to assure an unambiguous solution of $\psi(s)$, traditional 2-D PU methods generally assume that the absolute phase difference between the neighboring pixels is less than π, which is called the phase continuity assumption [5]. If it holds, the gradient of the ambiguity number of $\psi(s)$ is given by

$$k(s) - k(s-1) = \nabla(\varphi(s), \varphi(s-1)) \tag{2}$$

where the index s and $s-1$ is the general description of the neighboring pixels and $\nabla(\cdot)$ is an operator

$$\nabla(\varphi(s), \varphi(s-1)) = \begin{cases} 0, & |\varphi(s) - \varphi(s-1)| \le \pi \\ -1, & \varphi(s) - \varphi(s-1) > \pi \\ 1, & \varphi(s) - \varphi(s-1) < -\pi. \end{cases} \tag{3}$$

It is clear that if the phase gradients of any pairs of the neighboring pixels are correct in (2), we can simply use a 2-D integration along an arbitrary path to unwrap the phase. However, (2) will not work when the phase gradient assumption is not sustained, especially when the coherence of the interferogram is not ideal.

The existing 2-D PU methods can be generally classified into the path-following-based and optimization-based categories [5]. Because the estimation of (2) may contain some errors and the 2-D phase integration path is not unique, the fundamental principle of the path-following-based 2-D PU methods is to find the most likely integration path to avoid the gradient errors in (2). Many PU concepts, theorems, and methods follow this principle, e.g., the interferometric residue [6], the envelope-sparsity theorem [7], [8], and the branch-cut method [9]. The other category usually transforms the PU problem into an over-determined formula [10] and solves an over-determined equation using the optimization model, e.g., the L^p-norm model [11]. In fact, several 2-D PU methods can be classified into either category. For example, the minimum-cost flow (MCF) method [12] can be considered as an MCF model in transportation theory [13] to determine the integration path, or an L^1-norm optimization to minimize the difference between the gradients obtained by (2) and that of the PU solution.

However, as an ill-posed problem, the aforementioned PU methods mostly rely on the accuracy of (2). When overwhelming phase gradients cannot maintain phase continuity in the

input interferogram, and there is no other prior knowledge, 2-D PU algorithms may fail to resolve the phase map. On the other hand, prior knowledge such as a rough spatial distribution of the ground deformation can facilitate 2-D PU solution of originally unsolvable interferograms. Some researchers have demonstrated its feasibility. For example, Gao *et al.* [14] applies an external DEM to achieve the PU results in large-phase-gradient areas. In addition, Dai *et al.* [15] proposed a model-assist PU method using a mining deformation model to assist PU in a drastic subsiding mining site. Hu *et al.* [16] used interferograms with relatively shorter temporal intervals to obtain the first-order displacement velocities over a rapid settling tailings impoundment to reduce the fringes in interferograms with longer time spans, and then added the first-order displacements back after a robust PU solution. In this article, we propose a novel knowledge-aided InSAR PU approach, abbreviated as KAPU. KAPU can incorporate different kinds of prior knowledge from different sources simultaneously through an integer programming model. Beyond that, we provide the mathematical evidence that the constraint of the optimization model of KAPU is totally unimodular (the mathematical definition of the unimodularity is described in Appendix). Therefore, KAPU can be efficiently solved without bothering any constraints on the ambiguity number such as to be an integer. In this case, KAPU can ensure the congruency between the input interferometric fringes and the rewrapped fringes of the PU results. Theoretical analysis and extensive experimental results demonstrate that KAPU outperforms the existing representative model-based 2-D PU algorithms on InSAR DEM generation and surface deformation.

The rest of this article is organized as follows. Section II reviews the traditional 2-D PU. Section III demonstrates the KAPU method. Section IV illustrates the applications of KAPU on the real and simulated interferometric datasets. Section V makes a conclusion.

II. PU Background and Problem Analysis

In this section, we will review the traditional 2-D PU from the viewpoint of the path-following-based method. Because we cannot fully trust the phase gradient estimation from (2), we need to find the optimal 2-D integration path to minimize the effect caused by the potential phase gradient error. The traditional way is to first compute the residues by integrating the estimations obtained by (2) on every 2×2 pixel window in the interferogram, and then to determine the integration path deploying branch-cuts to balance the residues; the integration path is not allowed to cross any branch-cut [5]. The thorny issue is that there are usually multiple ways to balance the residues given an interferogram but InSAR cannot provide us enough information to determine which way is optimal. Therefore, the branch-cut is also named as the "ghost line" [6]. Even worse, although sometimes we know the most desirable way to balance the residues, the computation theory still does not allow us to implement the idea effectively.

For example, in the floodplain along the Coari River in Amazon, ALOS-2 PALSAR-2 ScanSAR images produce condensed interferometric fringes [Fig. 1(a)]. To ensure that the PU integration path climbs along the correct direction

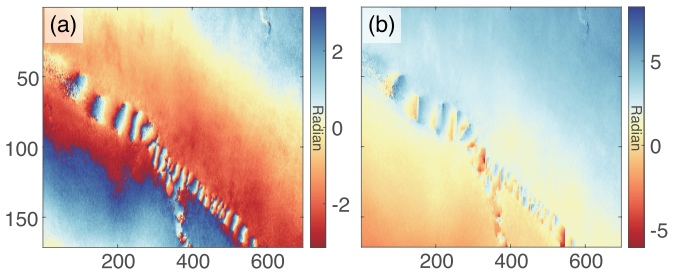

Fig. 1. (a) Interferogram generated from ALOS-2 PALSAR-2 SAR images over the floodplain in Amazon. (b) PU result obtained by MCF.

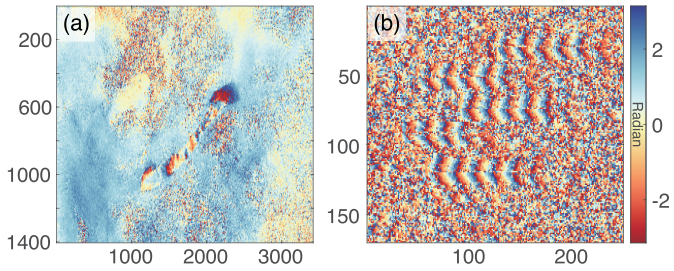

Fig. 2. (a) Interferogram generated from Sentinel-1 SAR images at the Slumgullion landslide, CO, USA. (b) Interferogram generated from COSMO-SkyMed SAR images at Lujiazui street, Shanghai, China.

of increasing phases, branch-cuts need to join the residues in "clumps" rather than pairs [17]. However, most of the traditional 2-D PU algorithms, except the L^0-norm PU strategy [17], prefer to build dipole cuts between each pair of residues if there is no extra guidance from PU weights. The unwrapped phase map obtained by the representative MCF method [12] is not continuous in the floodplain [Fig. 1(b)]. Although the L^0-norm PU strategy may give us the desired PU result for such condensed fringes, the L^0-norm PU problem is an NP-hard problem even without measuring bias [18], suggesting that any methods in polynomial time cannot generate an exact solution unless the P-problem set is equal to the NP-problem set. A polynomial-time algorithm means that its running time is upper bounded by a polynomial expression of the size of the input. The community of computer science believes that the polynomial-time algorithm can be practically implemented; however, if the P-problem set and the NP-problem set are not equivalent (widely believed), the solution of NP-hard problems requires an exhaustive search, which is significantly more difficult to compute than the polynomial-time algorithm [19]. This represents a common challenge in other InSAR applications. For example, Fig. 2(a) is the InSAR map of the Slumgullion landslide (CO, USA) deformation from Sentinel-1, and Fig. 2(b) is the InSAR map of the skyscrapers in Lujiazui street (Shanghai, China) from COSMO-SkyMed. Although the landscapes and objects in Figs. 1 and 2 differ, their interferometric fringes share similar patterns which require the phase integration paths to be along the "channel" direction. Therefore, if we only expect to solve 2-D PU problems through a model design based on the information from the interferogram, it may be too challenge to design the PU algorithm, i.e., assistance from the extra information is

desired in practice. In the next section, we will propose a novel Knowledge-Aided InSAR PU approach.

III. Design of KA

For simplicity, the general PU optimization model shown in (4)–(6) will be used in the discussion.

$$\arg \min_{k(s)} \sum_{(s,s-1)} w(s, s-1) \cdot f(t(s, s-1)) \tag{4}$$

$$\text{s.t. } k(s) - k(s-1) - \nabla(\varphi(s), \varphi(s-1)) = t(s, s-1) \tag{5}$$

$$k(s) \in \text{integer} \tag{6}$$

where $f(\cdot)$ is the objective function, $t(s, s-1)$ is the auxiliary variable and $w(s, s-1)$ is a weight coefficient (any features that characterize the quality of the input interferogram can be used as $w(s, s-1)$ [5]). The physical meaning of (4)–(6) is to minimize the difference between the unwrapped phase gradient $k(s)-k(s-1)$ and the estimated gradient $\nabla(\varphi(s), \varphi(s-1))$ to obtain the PU result under the objective function $f(\cdot)$. Most of the existing PU methods can be converted into (4)–(6) with different $f(\cdot)$s. For example, when $f(\cdot)$ is $|\cdot|$, (4)–(6) will be MCF.

It is straightforward that if the supplementary information can cover the whole InSAR imaging area, and the accuracy of the ambiguity number of the PU results estimated from the prior knowledge is less than one interferometric phase ambiguity (i.e., the supplementary information can clarify the benchmark $k(s)$ values of all pixels), the PU processing will be non-challenging with the flawless $k(s)$ values at all pixels. However, usually, the supplementary information to help a determination of the benchmark $k(s)$ values is only available at a limited number of pixels in the imagery (e.g., at GPS sites); additionally, the supplementary information may contain bias. Hence, we need to make full use of the supplementary information with (4)–(6) to obtain an enhanced PU solution, i.e.,

$$\arg \min_{k(s)} \sum_{(s,s-1)} w(s, s-1) \cdot f(t(s, s-1)) + \sum_{u} w(u) \cdot f(t(u)) \tag{7}$$

$$\text{s.t. } k(s) - k(s-1) - \nabla(\varphi(s), \varphi(s-1)) = t(s, s-1) \tag{8}$$

$$k(s), k(u) \in \text{integer} \tag{9}$$

$$k(u) - K(u) = t(u), \quad u \in \mathscr{K} \tag{10}$$

where $t(u)$ is the auxiliary variable and $w(u)$ is the weighted coefficient for pixel u, and $\mathscr{K}$ is the index set in which the pixels have the supplementary information of a known ambiguity number $K(u)$. The high-accuracy LiDAR DEMs, deformation models, pixel offset tracking results and GPS data may contribute to an estimation of $\mathscr{K}$. Taking the DEM generation as an example, assuming that the vertical height $h(u)$ of pixel u is known from the supplementary information, $K(u)$ is given by $\text{round}(h(u) \cdot B \cdot m)/(\lambda \cdot r \cdot \sin(\theta))$, where r is the slant range of the target, θ is the incidence angle, λ is the wavelength, and B is the normal baseline. Here m is the transmit-receive factor of the system: $m = 1$ represents the bistatic mode and $m = 2$ represents the distributed mode. The comparison

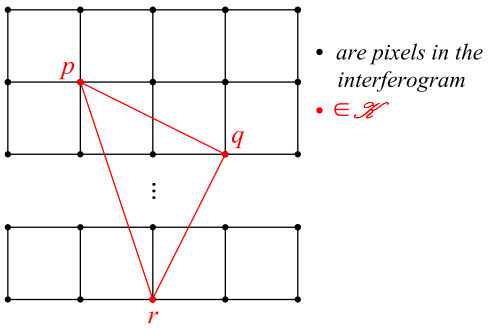

Fig. 3. Schematic view of the PU network of KAPU.

between (4)–(6) and (7)–(10) shows that the supplementary information is added as an additional constraint. The optimization theory demonstrates that the equality constraint [i.e., (10)] may not hurt the convexity (i.e., solvability) of the optimization model. The convex optimization can be solved by polynomial-time algorithms, whereas the mathematical optimization is generally NP-hard [20]. For example, the PU method proposed in [10] or the L^2-norm method with some approximate conditions [11] can directly apply (10). However, for PU methods, such as the MCF-framework-based methods, (10) will destroy the total unimodularity of the constraints. If the constraints of (7)–(10) are not totally unimodular, (9) cannot be removed without hurting the optimality, i.e., (7)–(10) will be an integer programming problem [20]. Under this condition, because of the existing of (9), the PU model transforms from a P problem to an NP-hard problem, i.e., we cannot find the optimal solution in polynomial time unless the P-problem set is equal to the NP-problem set. On the other hand, constraining the decision variables as the integer can keep the congruency between the input interferometric fringes and the rewrapped fringes of the PU result, i.e., overfreely removing (9) will result in the discontinuous phase gradient error spreading from the low-quality region to the whole interferogram [5], [6].

To solve this issue, we introduce $K(u)(u \in \mathscr{K})$ into (4)–(6) in a gradient form, i.e.,

$$\arg \min_{k(s)} \sum_{(s,s-1)} w(s, s-1) \cdot f(t(s, s-1)) + \sum_{(u,v)} w(u, v) \cdot f(t(u, v)) \tag{11}$$

$$\text{s.t. } k(s) - k(s-1) - \nabla(\varphi(s), \varphi(s-1)) = t(s, s-1) \tag{12}$$

$$k(s), k(u), k(v) \in \text{integer} \tag{13}$$

$$k(u) - k(v) - (K(u) - K(v)) = t(u, v), \quad u, v \in \mathscr{K} \tag{14}$$

where $t(u, v)$ is the auxiliary variable and $w(u, v)$ is the weighted coefficient for pixels u and v. Since $(K(u) - K(v))$ is more reliable than $\nabla(\varphi(s), \varphi(s-1))$, we can tolerate a larger $w(u, v)$ than $w(s, s-1)$. For example, if the supplementary information is absolutely trustworthy, $w(u, v)$ can be larger than $\sum_{(s,s-1)} w(s, s-1)$. It suggests that individual $t(u, v)$ has a greater impact on the objective function than all

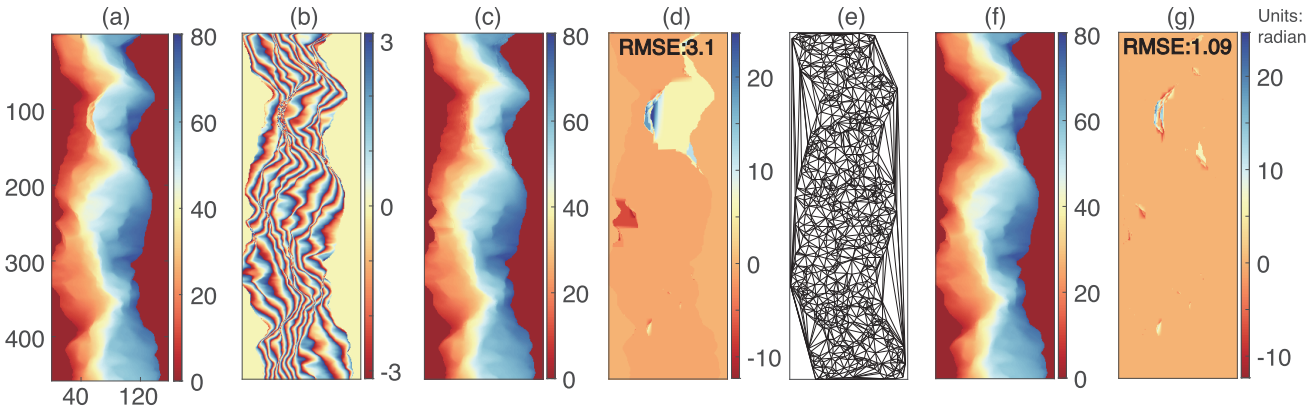

Fig. 4. (a) Reference unwrapped phase. (b) Simulated interferogram of (a). (c) PU result of (a) obtained by MCF. (d) Misfits between (a) and (c). (e) Network of $\mathscr{K}$ with probability (1/50). (f) PU result of (a) obtained by KAPU. (g) Misfits between (a) and (f). RMSE represents the root-mean-square-error.

$t(s, s-1)$ together. The beauty of (11)–(14) is that its equivalent constraint is totally unimodular as long as the gradient field described in (14) is closed, even if the pixels u and v are not neighbors in the regular grid-network. The closed gradient field means that every pixel in this field is included in a cycle, which is a nonempty trail in which the only repeated vertices are the first and last vertices as defined in the graph theory [13]. For instance, Fig. 3 shows the schematic view when pixels p, q, and r have prior knowledge available, so there will be three constraints in (14) given by $k(p)-k(q)-(K(p)-K(q)) = t(p,q)$, $k(q)-k(r)-(K(q)-K(r)) = t(q,r)$ and $k(r)-k(p)-(K(r)-K(p)) = t(r,p)$. Fig. 3 states that the PU model of KAPU is designed on a bi-level network from (12) and (14), respectively, so the network generated by $\mathscr{K}$ can provide more options on the ideal integration path for PU. For example, besides the regular neighboring pixels on a grid network, the pixel p has alternative options on the integration path to reach pixels q or r. In addition, since the supplementary information can break up the limits of the phase continuity assumption, the gradient estimated by $\mathscr{K}$ (i.e., $K(u)-K(v)$) can be any integer. Due to the total unimodularity, (14) is applicable in most MCF-framework-based PU methods (e.g., MCF [12], statistical-cost, network-flow PU algorithm (SNAPHU) [21] and minimum infinity-norm-based method (MIN) [22]) without losing solvability. It is noticeable that if the pixels in $\mathscr{K}$ are sparse, the triangulated irregular network, usually an intermediate product of Persistent Scatterer InSAR (PSInSAR) [23], can be used to generate the phase gradient map to ensure path closure. The mathematical proof of the total unimodularity of the constraints in (11)–(14) is shown in Appendix. It is worth to mention that since KAPU belongs to the PU optimization framework, which compiles prior knowledge from different sources with InSAR observations, its time and space complexities are different considering different objective functions, i.e., $f(\cdot)$ in (11). For example, if $f(\cdot)$ is $|\cdot|$, its time and space complexities are equivalent to those of the MCF method because the constraint of KAPU is totally unimodular. However, because KAPU considers the supplementary information, its problem size (the number of the variables and constraints in (11)–(14) will be larger than those of traditional 2-D PU methods.

IV. Performance Analysis

We test the effectiveness of KAPU with the L^1-norm objective function (i.e., $f(\cdot)$ is $|\cdot|$) using three experiments. In the first experiment, we analyze the effectiveness of KAPU with different sizes of $\mathscr{K}$s. The second experiment focuses on the performance of KAPU on the DEM generation from single-pass TanDEM-X InSAR data. Finally, the third experiment tests the PU accuracy of KAPU on the deformation detection using Sentinel-1 InSAR data.

Fig. 4(a) shows the reference unwrapped phase in the first experiment in the mountainous areas in the Isolation Peak in Colorado, USA. Fig. 4(b) is the simulated noise-free interferogram of Fig. 4(a). Fig. 4(c) is the PU result of the representative MCF PU method. Fig. 4(d) shows the misfits between Fig. 4(a) and (c). The interferometric fringes in Fig. 4(b) is complicated even without phase noise, which is apparently difficult for the traditional MCF PU method simply based on the phase continuity assumption. However, if we randomly pick up pixels in Fig. 4(a) with a probability of (1/50) (i.e., one out of every 50 pixels) to constitute a closed network of $\mathscr{K}$ [Fig. 4(e)], the consequent KAPU result is shown in Fig. 4(f). Fig. 4(g) shows the misfits between Fig. 4(a) and (f). The same reference point and range of the color bar have been applied in the PU results [Fig. 4(c) and (f)] and PU misfits [Fig. 4(d) and (g)] (same for the following experiments). We can see that, with knowledge-aided information of $\mathscr{K}$, KAPU is superior to the traditional MCF PU method. Fig. 5(a) and (b) illustrates the closed PU networks of $\mathscr{K}$ with probabilities of (1/100) and (1/500) respectively, and their PU results of KAPU are shown in Fig. 5(c) and (d). Parts (e) and (f) of Fig. 5 are the misfits between Figs. 4(a) and 5(c), and Fig. 4(a) and (d), respectively. It can be seen that the smaller the size of $\mathscr{K}$, the worse the PU performance of KAPU will be. However, the accuracy of KAPU is still better than that achieved without the assistance of $\mathscr{K}$.

The second experiment is performed on a single-pass TanDEM-X MB dataset acquired on October 21, 2012, for DEM generation in Weinan, Shaanxi, China. Fig. 6(a) shows the flattened and filtered interferogram of the study area. This area is featured in mountainous and rugged landscapes.

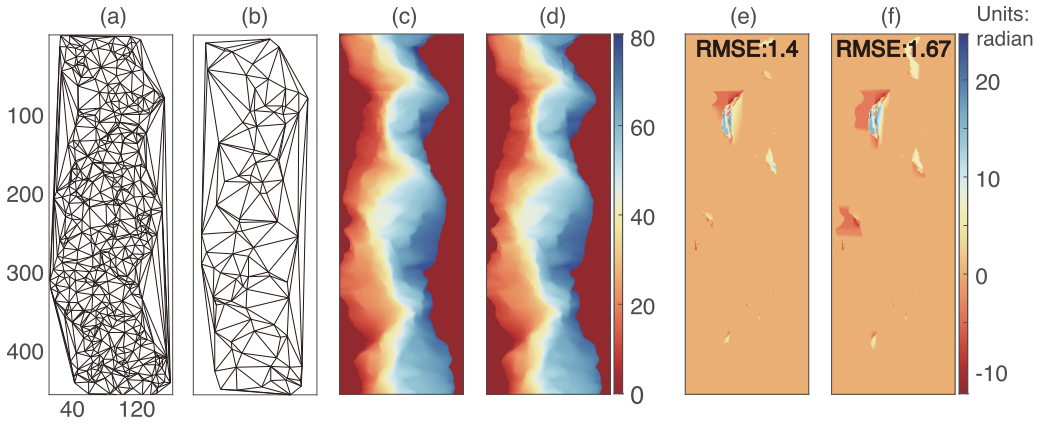

Fig. 5. (a) Network of $\mathscr{K}$ with probability (1/100). (b) Network of $\mathscr{K}$ with probability (1/500). (c) PU result of Fig. 4(a) obtained by KAPU with using (a). (d) PU result of Fig. 4(a) obtained by KAPU with using (b). (e) Misfits between Fig. 4(a) and (c). (f) Misfits between Fig. 4(a) and (d).

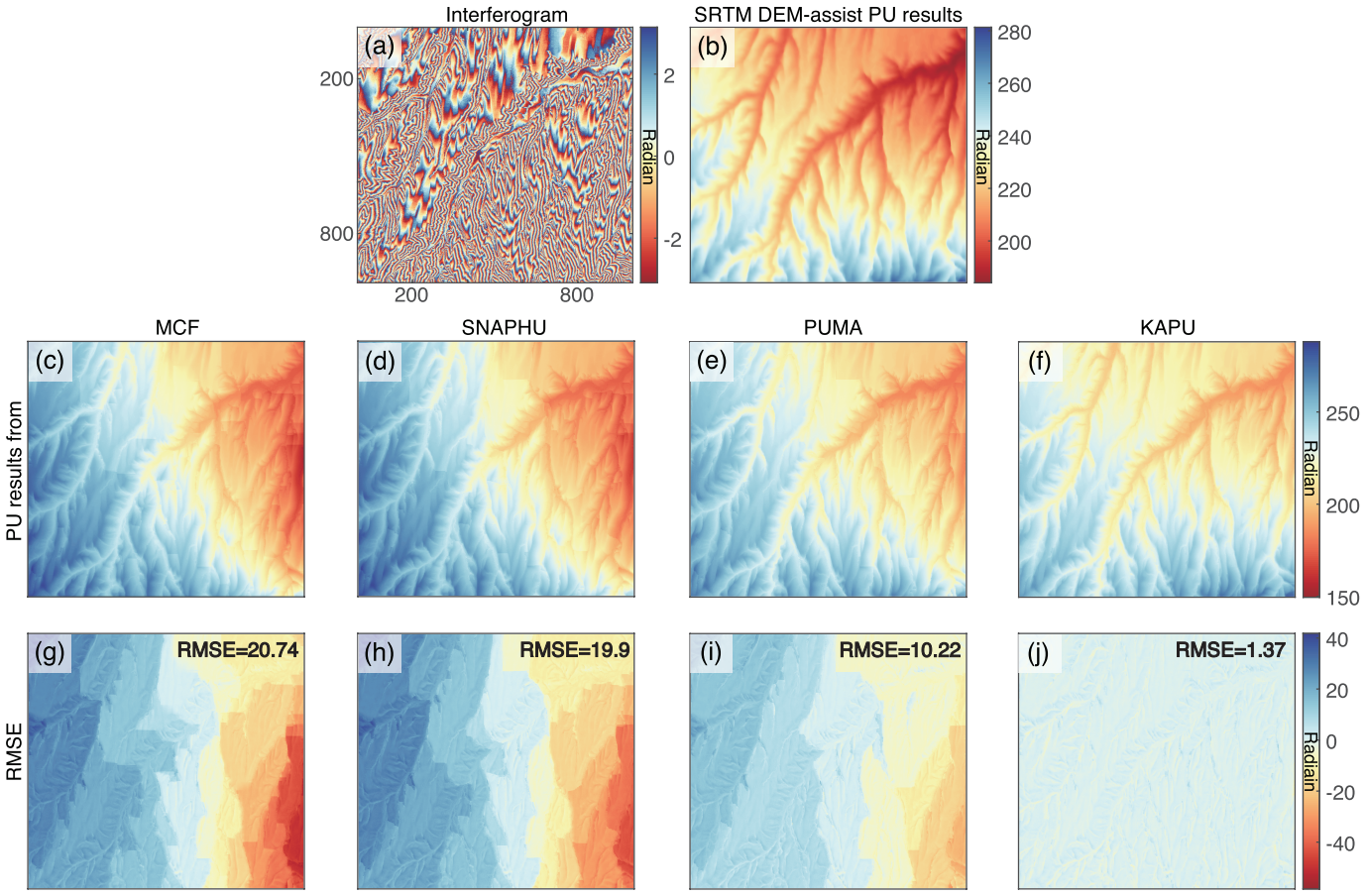

Fig. 6. (a) TanDEM-X interferogram. (b) Reference PU result of (a) obtained from SRTM DEM. (c) PU result of (a) obtained by MCF. (d) PU result of (a) obtained by SNAPHU. (e) PU result of (a) obtained by PUMA. (f) PU result of (a) obtained by KAPU. (g) Difference between (b) and (c). (h) Difference between (b) and (d). (i) Difference between (b) and (e). (j) Difference between (b) and (f).

The phase continuity assumption cannot sustain at such a steep topographic gradient, leading to an incorrect PU result using the traditional 2-D PU methods. Fig. 6(b) shows the reference unwrapped phase of Fig. 6(a) generated by the Shuttle Radar Topography Mission (SRTM) DEM. Fig. 6(c)–(f) shows PU results obtained by the MCF [12], SNAPHU [21], PU-max-flow (PUMA) [24], and our proposed KAPU methods, respectively. The statistical cost mode of SNAPHU is set to "TOPO," the clique potential exponent of PUMA is set to be 0.5. Here, we randomly select pixels in Fig. 6(b) with a probability of (1/100) to generate a closed network of $\mathscr{K}$ for KAPU. Fig. 6(g)–(j) shows the PU misfits between Fig. 6(b)–(f). As a result of the complicated and dense interferometric fringes in Fig. 6(a), the phase continuity assumption

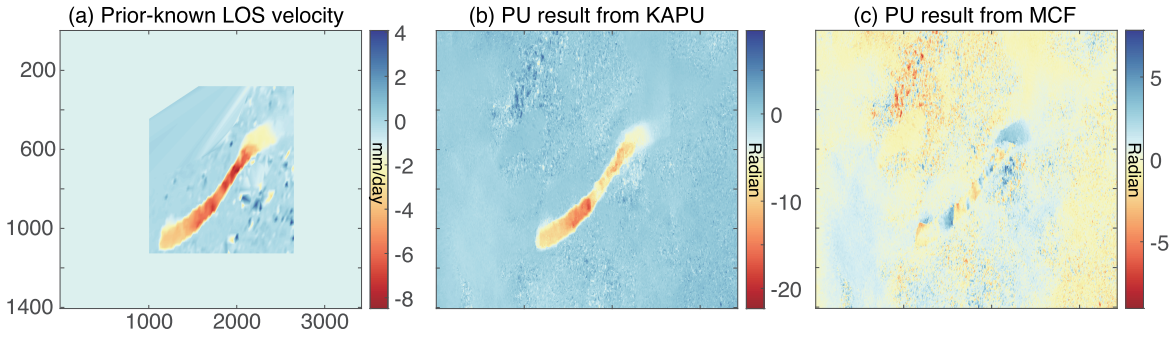

Fig. 7. (a) Deformation speed estimated by UAVSAR pixel offset tracking. (b) PU result of Fig. 2(a) obtained by KAPU. (c) PU result of Fig. 2(a) obtained by MCF.

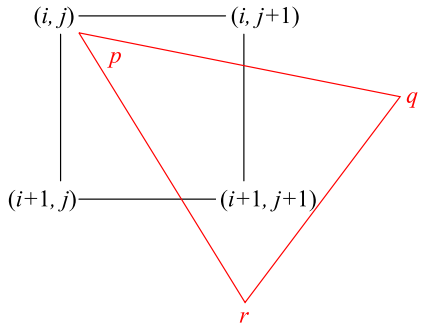

Fig. 8. Sketch map illustrating the meanings of the variables in (15)–(18) in which $\{(s, s-1)|(((i, j), (i, j+1)), ((i, j), (i+1, j)), ((i+1, j), (i+1, j+1)), ((i, j+1), (i+i, j+1)))\}$ and $\{(u, v)|((p, q), (q, r), (p, r))\}$.

is violated. Consequently, several obvious PU errors stick out in some areas [Fig. 6(g)–(i)]. Because the phase gradients from $\mathscr{K}$ can effectively rectify the incorrect gradients estimated by (2), KAPU significantly outperforms three representative 2-D PU methods.

The third experiment is on the Slumgullion landslide deformation mapping in Colorado, USA [25]–[28]. Slumgullion is a natural laboratory with continuous motions for the past 300 years since its reactivation. The fastest segment occurs at the narrow neck of the landslide at dozens of millimeters per day in a short width of $<$ 200 m. Such a high phase gradient exceeds the InSAR resolvability of Sentinel-1 data at 12-day intervals. Taking advantage of the submeter-to-meter high-resolution and four distinct flight lines of NASA/JPL's airborne UAVSAR system, the complete 3-D displacements have been achieved by hybrid pixel offset tracking and InSAR method [29] or the pixel offset tracking method alone [30]. The latter method provides 3-D displacements at a higher resolution without sacrificing for InSAR coherence while the SNR is lower due to less input. Here, we opt for the higher resolution results to compute the corresponding displacement along the Sentinel-1 line-of-sight (LOS) [Fig. 2(a)]. The two Sentinel SAR images acquired on August 13, 2018, and August 25, 2018, are used to generate the interferogram [Fig. 2(a)]. In this experiment, the assisting knowledge is the deformation speed at mm/day shown in Fig. 7(a) (the absolute phase can be estimated using "deformation speed $\times$ time interval of SAR images $\times$ (4π /Wavelength $= 0.0555$ m)"), which is achieved by the UAVSAR pixel offset tracking method (resampled and interpolated) [29]. With a random choice of pixels with a probability of (1/100) for generating $\mathscr{K}$ of KAPU from Fig. 7(a) and (b) is the PU result of the 12-day interferogram [Fig. 2(a)] obtained by KAPU. Fig. 7(c) is the PU result of Fig. 2(a) obtained by the MCF method. The comparison between Fig. 7(b) and (c) shows that MCF is unable to unwrap the phases continuously in this landslide area, but the KAPU result illustrates a smooth spatial variation crossing the active landslide body. It approves that the auxiliary information provided by $\mathscr{K}$ can effectively assist (11)–(14) to pick up a more robust phase integration path.

V. Conclusion

2-D PU is a critical step in InSAR processing. As an ill-posed problem, how to reduce the nondeterminacy of 2-D PU has been a longstanding challenge in InSAR applications. To solve this issue, here we propose an effective knowledge-aided 2-D PU framework (KAPU) to fuse the auxiliary information from different remote sensing sensors from the air and space. We would like to highlight that since the constraint of KAPU is totally unimodular, this method ensures the congruency between the input interferometric fringes and the rewrapped fringes of the PU results. Three experimental results are presented to verify that KAPU can incorporate the elevation or deformation knowledge from other remote sensing sensors and methods, so as to break up the limits of the phase continuity assumption and to enhance the 2-D PU solutions in previously theoretically and practically infeasible scenarios. This improvement enormously broadens the scope of InSAR applications.

In this article, KAPU is described from the perspective of the optimization-based PU method. However, KAPU can keep the fringe congruency, so KAPU can also be considered as a path-following-based method. In the future, we would like to investigate how to translate the residue concept with the bi-level network applied in KAPU and to compile representative path-following-based PU methods into the KAPU framework.

Appendix

In Appendix, we will prove the total unimodularity of (12) and (14) under the framework of MCF, i.e., $f(\cdot)$ is $|\cdot|$.

$$\arg\ \min \sum_{(s,s-1)} w(s,s-1)\cdot(t^+(s,s-1)+t^-(s,s-1))+\sum_{(u,v)} w(u,v)\cdot(t^+(u,v)+t^-(u,v)) \tag{15}$$

$$\begin{aligned}\text{s.t. } & t^-((i,j+1),(i,j))-t^+((i,j+1),(i,j))+t^-((i+1,j+1),(i,j+1))-t^+((i+1,j+1),(i,j+1))\\ & +t^-((i+1,j),(i+1,j+1))-t^+((i+1,j),(i+1,j+1))+t^-((i,j),(i+1,j))-t^+((i,j),(i+1,j))=\\ & \nabla(\varphi(i,j+1),\varphi(i,j))+\nabla(\varphi(i+1,j+1),\varphi(i,j+1))+\nabla(\varphi(i+1,j),\varphi(i+1,j+1))+\nabla(\varphi(i,j),\varphi(i+1,j))\end{aligned} \tag{16}$$

$$t^+(p,q)-t^-(p,q)+t^+(q,r)-t^-(q,r)+t^+(r,p)-t^-(r,p)=0 \tag{17}$$

$$t^+(s,s-1)\geq 0,\quad t^-(s,s-1)\geq 0,\ t^+(u,v)\geq 0,\ t^-(u,v)\geq 0 \tag{18}$$

The unimodularity means that every square sub-matrix of the equivalent coefficient matrix of (12) and (14) has a determinant of -1, 0 or $+1$ [20]. We assume that the closure requirement of $\mathscr{K}$ is satisfied by the triangulated irregular network; any kind of closed network will not change the proof. Considering the neighboring pixels shown in Fig. 8, each link in Fig. 8 corresponds to a constraint in (12) and (14). Since a decision variable which is unrestricted in the absolute operation can be modeled linearly by considering it as the difference of two nonnegative variables [20], we can linearize (11) by allowing for $|t(s,s-1)|=t^+(s,s-1)+t^-(s,s-1)$, $t(s,s-1)=t^+(s,s-1)-t^-(s,s-1)$, $|t(u,v)|=t^+(u,v)+t^-(u,v)$ and $t(u,v)=t^+(u,v)-t^-(u,v)$, where $t^+(s,s-1)$, $t^-(s,s-1)$, $t^+(u,v)$ and $t^-(u,v)$ are additional auxiliary variables. And then if we add the constraints of the neighboring pixels in each close set, (11)–(14) are equivalent to (15)–(18), as shown at the top of the page.

As follows, we will prove the coefficient matrix of (16) and (17) is total unimodular using the reduction to absurdity. By contradiction, there are sub-matrix of the coefficient matrix of (16) and (17) whose determinant is not -1, 0 or $+1$. Among them, we consider B with the minimum matrix-size $M\times M$. Because every element in the coefficient matrix of (16) and (17) is -1, 0 or $+1$, as $M>1$, i.e., the number of the non-zero elements in a column in the matrix B will be 0, 1 or 2. It is clear that if there is a column without nonzero element, the determinant of B is 0. If there is a column with one non-zero element $a\in\{+1,-1\}$, the determinant of B will be the product of a and its cofactor. Because the size of the cofactor of a is less than M, its value must be -1, 0 or $+1$, so that the product of a and its cofactor must be -1, 0 or $+1$. If each column of B has two non-zero elements $a_i(i=1,2)$, and we know $a_1+a_2=0$, then B is singular whose determinant is 0. Therefore, B does not exist so the coefficient matrix of (16) and (17) is totally unimodular.

REFERENCES

[1] M. Xing, V. Pascazio, and H. Yu, "A special issue on synthetic aperture radar interferometry," *IEEE Geosci. Remote Sens. Mag.*, vol. 8, no. 1, pp. 6–7, Mar. 2020.

[2] R. Bamler and P. Hartl, "Synthetic aperture radar interferometry," *Inverse Problems*, vol. 14, no. 4, pp. R1–R54, Aug. 1998.

[3] P. A. Rosen *et al.*, "Synthetic aperture radar interferometry," *Proc. IEEE*, vol. 88, no. 3, pp. 333–382, Mar. 2000.

[4] P. Berardino, G. Fornaro, R. Lanari, and E. Sansosti, "A new algorithm for surface deformation monitoring based on small baseline differential SAR interferograms," *IEEE Trans. Geosci. Remote Sens.*, vol. 40, no. 11, pp. 2375–2383, Nov. 2002.

[5] H. Yu, Y. Lan, Z. Yuan, J. Xu, and H. Lee, "Phase unwrapping in InSAR: A review," *IEEE Geosci. Remote Sens. Mag.*, vol. 7, no. 1, pp. 40–58, Mar. 2019.

[6] D. C. Ghiglia and M. D. Pritt, *Two-Dimensional Phase Unwrapping: Theory, Algorithms, and Software*. New York, NY, USA: Wiley, 1998.

[7] H. Yu, Y. Lan, J. Xu, D. An, and H. Lee, "Large-scale L0-norm and L1-norm two-dimensional phase unwrapping," *IEEE Trans. Geosci. Remote Sens.*, vol. 55, no. 8, pp. 4712–4728, Aug. 2017.

[8] H. Yu, Y. Zhou, S. S. Ivey, and Y. Lan, "Large-scale multibaseline phase unwrapping: Interferogram segmentation based on multibaseline envelope-sparsity theorem," *IEEE Trans. Geosci. Remote Sens.*, vol. 57, no. 11, pp. 9308–9322, Nov. 2019.

[9] R. M. Goldstein, H. A. Zebker, and C. L. Werner, "Satellite radar interferometry: Two-dimensional phase unwrapping," *Radio Sci.*, vol. 23, no. 4, pp. 713–720, Jul. 1988.

[10] H. Yu, Z. Li, and Z. Bao, "Residues cluster-based segmentation and outlier-detection method for large-scale phase unwrapping," *IEEE Trans. Image Process.*, vol. 20, no. 10, pp. 2865–2875, Oct. 2011.

[11] D. C. Ghiglia and L. A. Romero, "Minimum Lp-norm two-dimensional phase unwrapping," *J. Opt. Soc. Amer. A, Opt. Image Sci.*, vol. 13, no. 10, pp. 1999–2013, Oct. 1996.

[12] M. Costantini, "A novel phase unwrapping method based on network programming," *IEEE Trans. Geosci. Remote Sens.*, vol. 36, no. 3, pp. 813–821, May 1998.

[13] R. K. Ahuja, T. L. Magnanti, and J. B. Orlin, *Network Flows: Theory, Algorithms and Applications*. Upper Saddle River, NJ, USA: Prentice-Hall, 1993.

[14] Y. Gao *et al.*, "A phase slicing 2-D phase unwrapping method using the L^1-norm," *IEEE Geosci. Remote Sens. Lett.*, early access, Sep. 30, 2020, doi: 10.1109/LGRS.2020.3025939.

[15] Y. Dai, A. H.-M. Ng, H. Wang, L. Li, L. Ge, and T. Tao, "Modeling-assisted InSAR phase-unwrapping method for mapping mine subsidence," *IEEE Geosci. Remote Sens. Lett.*, early access, May 14, 2020, doi: 10.1109/LGRS.2020.2991687.

[16] X. Hu, T. Oommen, Z. Lu, T. Wang, and J.-W. Kim, "Consolidation settlement of salt lake county tailings impoundment revealed by time-series InSAR observations from multiple radar satellites," *Remote Sens. Environ.*, vol. 202, pp. 199–209, Dec. 2017.

[17] A. Ferretti, A. M. Guarnieri, C. Prati, and F. Rocca, *InSAR Principles: Guidelines for SAR Interferometry Processing and Interpretation*. Noordwijk The Netherlands: ESA Publications, 2007.

[18] C. W. Chen and H. A. Zebker, "Network approaches to two-dimensional phase unwrapping: Intractability and two new algorithms," *J. Opt. Soc. Amer. A, Opt. Image Sci.*, vol. 17, no. 3, pp. 401–414, Mar. 2000.

[19] M. Sipser, *Introduction to the Theory of Computation*, 2nd ed. Boston, MA, USA: Thomson Course Technology, 2006.

[20] D. J. Rader, *Deterministic Operations Research: Models and Methods in Linear Optimization*. Hoboken, NJ, USA: Wiley, 2010.

[21] C. W. Chen and H. A. Zebker, "Two-dimensional phase unwrapping with use of statistical models for cost functions in nonlinear optimization," *J. Opt. Soc. Amer. A, Opt. Image Sci.*, vol. 18, no. 2, pp. 338–351, 2001.

[22] H. Yu, Y. Lan, H. Lee, and N. Cao, "2-D phase unwrapping using minimum infinity-norm," *IEEE Geosci. Remote Sens. Lett.*, vol. 15, no. 12, pp. 1887–1891, Dec. 2018.

[23] F. Xue, X. Lv, F. Dou, and Y. Yun, "A review of time-series interferometric SAR techniques: A tutorial for surface deformation analysis," *IEEE Geosci. Remote Sens. Mag.*, vol. 8, no. 1, pp. 22–42, Mar. 2020.

[24] J. M. Bioucas-Dias and G. Valadao, "Phase unwrapping via graph cuts," *IEEE Trans. Image Process.*, vol. 16, no. 3, pp. 698–709, Mar. 2007.

[25] N. Cao *et al.*, "Airborne DInSAR results using time-domain backprojection algorithm: A case study over the Slumgullion landslide in Colorado with validation using spaceborne SAR, airborne LiDAR, and ground-based observations," *IEEE J. Sel. Topics Appl. Earth Observ. Remote Sens.*, vol. 10, no. 11, pp. 4987–5000, Nov. 2017.
[26] B. G. Delbridge, R. Bürgmann, E. Fielding, S. Hensley, and W. H. Schulz, "Three-dimensional surface deformation derived from airborne interferometric UAVSAR: Application to the Slumgullion landslide," *J. Geophys. Res., Solid Earth*, vol. 121, no. 5, pp. 3951–3977, May 2016.
[27] P. Milillo, E. J. Fielding, W. H. Shulz, B. Delbridge, and R. Burgmann, "COSMO-SkyMed spotlight interferometry over rural areas: The Slumgullion landslide in Colorado, USA," *IEEE J. Sel. Topics Appl. Earth Observ. Remote Sens.*, vol. 7, no. 7, pp. 2919–2926, Jul. 2014.
[28] W. H. Schulz, J. W. Kean, and G. Wang, "Landslide movement in Southwest Colorado triggered by atmospheric tides," *Nature Geosci.*, vol. 2, no. 12, pp. 863–866, Dec. 2009.
[29] X. Hu, R. Bürgmann, W. H. Schulz, and E. J. Fielding, "Four-dimensional surface motions of the Slumgullion landslide and quantification of hydrometeorological forcing," *Nature Commun.*, vol. 11, no. 1, pp. 1–9, Jun. 2020.
[30] X. Hu, R. Bürgmann, E. J. Fielding, and H. Lee, "Internal kinematics of the Slumgullion landslide (USA) from high-resolution UAVSAR InSAR data," *Remote Sens. Environ.*, vol. 251, Dec. 2020, Art. no. 112057.

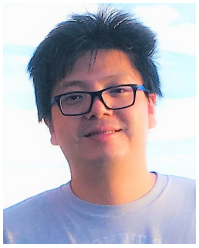

Hanwen Yu (Senior Member, IEEE) received the B.S. and Ph.D. degrees in electronic engineering from Xidian University, Xi'an, China, in 2007 and 2012, respectively.

He was a Post-Doctoral Research Fellow with the Department of Civil and Environmental Engineering, National Center for Airborne Laser Mapping, University of Houston, Houston, TX, USA. He is a Full Professor with the School of Resources and Environment, University of Electronic Science and Technology of China, Chengdu, China. He has authored or coauthored more than 35 research articles in high-impact peer-reviewed journals, such as the IEEE TRANSACTIONS ON GEOSCIENCE AND REMOTE SENSING, the IEEE TRANSACTIONS ON IMAGE PROCESSING, and *Remote Sensing of Environment*. He has reviewed more than 200 manuscripts for over 20 different journals. His research interests include phase unwrapping, machine learning, and synthetic aperture radar (SAR) interferometry (InSAR) signal processing and applications.

Prof. Yu was a recipient of the Recognition of Best Reviewer of the IEEE TRANSACTIONS ON GEOSCIENCE AND REMOTE SENSING in 2019. He serves as a Topical Associate Editor for the IEEE TRANSACTIONS ON GEOSCIENCE AND REMOTE SENSING, and an Associate Editor for the *IEEE Geoscience and Remote Sensing Magazine*. He has guest edited five special issues on InSAR remote sensing for different journals (e.g., IEEE JOURNAL OF SELECTED TOPICS IN APPLIED EARTH OBSERVATIONS AND REMOTE SENSING and MDPI *Sensors*).

Xie Hu (Member, IEEE) received the bachelor's degree in geographic information system from the China University of Geosciences, Wuhan, China, in 2011, the M.Eng. degree in photogrammetry and remote sensing from Wuhan University, Wuhan, and the Dr. Phil. degree in geophysics from Southern Methodist University, Dallas, TX, USA, in 2018.

She was a Post-Doctoral Research Fellow with the University of California, Berkeley, Berkeley, CA, USA, from 2018 to 2020. She is an Assistant Professor of Geosensing with the University of Houston, Houston, TX, USA. Her research interests include SAR remote sensing techniques and applications in geological hazards and the Earth's shallow processes.

Dr. Hu was awarded the NASA Earth and Space Science Fellowship in 2015 and the NASA New (Early Career) Investigator Program in Earth Science in 2021.